Higher-Order Weyl Semimetals

Sayed Ali Akbar Ghorashi,[1,*] Tianhe Li,[2] and Taylor L. Hughes[2]
[1]Department of Physics, William & Mary, Williamsburg, Virginia 23187, USA
[2]Department of Physics and Institute for Condensed Matter Theory, University of Illinois at Urbana-Champaign, Illinois 61801, USA

(Received 14 July 2020; accepted 1 December 2020; published 31 December 2020)

We investigate higher-order Weyl semimetals (HOWSMs) having bulk Weyl nodes attached to both surface and hinge Fermi arcs. We identify a new type of Weyl node, which we dub a 2nd-order Weyl node, that can be identified as a transition in momentum space in which both the Chern number and a higher order topological invariant change. As a proof of concept we use a model of stacked higher order quadrupole insulators (QI) to identify three types of WSM phases: 1st order, 2nd order, and hybrid order. The model can also realize type-II and hybrid-tilt WSMs with various surface and hinge arcs. After a comprehensive analysis of the topological properties of various HOWSMs, we turn to their physical implications that show the very distinct behavior of 2nd-order Weyl nodes when they are gapped out. We obtain three remarkable results: (i) the coupling of a 2nd-order Weyl phase with a conventional 1st-order one can lead to a hybrid-order topological insulator having coexisting surface cones and flat hinge arcs that are independent and not attached to each other. (ii) A nested 2nd-order inversion-symmetric WSM by a charge-density wave (CDW) order generates an insulating phase having coexisting flatband surface and hinge states all over the Brillouin zone. (iii) A CDW order in a time-reversal symmetric higher-order WSM gaps out a 2nd-order node with a 1st-order node and generates an insulating phase having coexisting surface Dirac cone and hinge arcs. Moreover, we show that a measurement of charge density in the presence of magnetic flux can help to identify some classes of 2nd-order WSMs. Finally, we show that periodic driving can be utilized as a way for generating HOWSMs. Our results are relevant to metamaterials as well as various phases of Cd_3As_2, KMgBi, and rutile-structure PtO_2 that have been predicted to realize higher order Dirac semimetals.

DOI: 10.1103/PhysRevLett.125.266804

Introduction.—Recently, a new family of topological crystalline phases that admit a higher-order bulk-boundary correspondence has been discovered. They have been dubbed higher-order symmetry protected topological (HOSPT) phases [1–35], and the hallmark of nth-order HOSPT phases is the existence of gapless states (or other observable topological features) on boundaries having codimension $d_c = n$. In this classification the conventional topological insulator phases are *1st order*. Moreover, the coexistence of, for example, $d_c = n - 1$ and $d_c = n$ boundary modes has been explored and is usually referred to as hybrid-order topology [36–39]. In addition to HOSPTs, very recent works have explored higher-order topological semimetals, that are often characterized by their hinge states [28,39–46], but so far these works have primarily focused on Dirac-like semimetal systems. In this Letter, we instead identify a type of higher-order Weyl semimetal (HOWSM): a class of semimetals which consists of at least a pair of what we will call 2nd-order Weyl nodes in the bulk. In addition to attached surface Fermi arcs, 2nd-order Weyl nodes have Fermi hinge arcs attached too. This is distinct from the case of higher-order Dirac semimetals (HODSMs), where the possible appearance of surface states is not related to the topology of the bulk Dirac nodes, i.e., they are not required to connect to the projections of the bulk Dirac nodes on the surfaces, but are instead associated to the topology in high-symmetry planes [39,40,42].

Here, we will characterize HOWSMs using symmetry considerations, momentum-resolved topological invariants, and their energy spectra. We present models of HOWSMs that can be easily tuned to 1st-order, 2nd-order, and hybrid-order WSMs (the latter where both 1st- and 2nd-order nodes coexist). Moreover, our models also allow for tilted Weyl cones that can be tuned to be type I, type II, or hybrid tilt [47,48]. We investigate multiple scenarios of which 2nd-order WSM are gapped out and obtain following remarkable results which *uniquely* characterizes these systems: (i) when a 2nd-order WSM is gapped out in the bulk by a 1st-order WSM, the hybridized system is an insulating phase having hybrid-order topology and exhibits a coexistence of independent Dirac cones on the surfaces and flatband Fermi arcs on the hinges and (ii) a charge-density wave (CDW) order in inversion and (iii) time-reversal symmetric 2nd-order WSMs induces an insulating phases having coexisting surface and hinge arcs throughout

the BZ and coexisting surface Dirac cone and hinge arcs, respectively. In addition, we explore the electromagnetic response of HOWSMs and find that in the presence of magnetic flux a local measurement of charge density can characterize the existence of a 2nd-order WSMs. Finally, we propose that circularly polarized light, or an analogous periodic drive, can generate HOWSMs in solid state systems and metamaterials.

Model and formalism.—We start with a simple model for HODSMs using spinless fermions from Ref. [39]:

$$H_{\mathrm{HODSM}}(\boldsymbol{k}) = \left(\gamma_x + \frac{1}{2}\cos k_z + \cos k_x\right)\Gamma_4 + \sin k_x \Gamma_3 + \left(\gamma_y + \frac{1}{2}\cos k_z + \cos k_y\right)\Gamma_2 + \sin k_y \Gamma_1, \tag{1}$$

where $\gamma_{x,y}$ represent the intracell coupling along x, y, $\{\Gamma_\alpha\}$ are direct products of Pauli matrices, σ_i, κ_i, following $\Gamma_0 = \sigma^3\kappa^0, \Gamma_i = -\sigma^2\kappa^i$ for $i = 1,\ 2,\ 3$, and $\Gamma_4 = \sigma^1\kappa^0$. The corresponding lattice basis configuration is specified in Fig. 1(a). Without loss of generality, we have set the amplitudes of intercell hoppings to 1, and will work in the C_4^z symmetric limit, $\gamma_x = \gamma_y = \gamma$. In addition to the C_4^z symmetry, the model in Eq. (1) has mirror symmetries $\mathcal{M}_x = \sigma^1\kappa^3$, $\mathcal{M}_y = \sigma^1\kappa^1$, $\mathcal{M}_z = I$, inversion symmetry $\mathcal{I} \equiv \mathcal{M}_x\mathcal{M}_y\mathcal{M}_z = \sigma^0\kappa^2$, and spinless time-reversal $\mathcal{T} = K$.

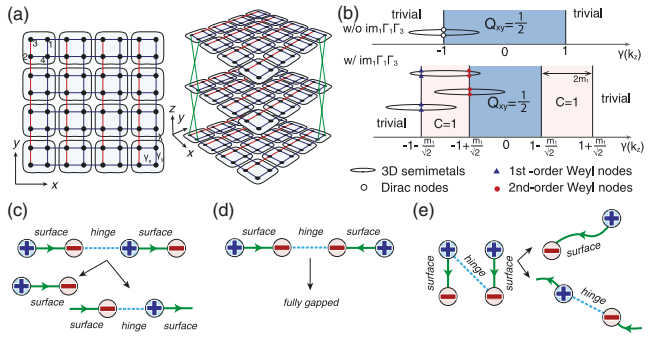

FIG. 1. (a) The lattice configuration of the HODSM model, which is constructed by stacking QIs. (b) Phase diagram of the 2D QI with (lower panel) or without (upper panel) the perturbation $m_1 i\Gamma_1\Gamma_3$ as a function of the intracell coupling $\gamma(k_z)$. The vertical direction is added as a visual aid; as such, the narrow loops represent various 3D higher-order semimetals. The loop in the top panel is a HODSM, loops from bottom to top in the bottom panel are 1st-order, 2nd-order, and hybrid-order HOWSMs. (c)–(e) The schematics of three arrangements of Weyl nodes in momentum space corresponding to (c) H^1, (d) H^2, and (e) H^3. Starting from a hybrid-topology WSM in $H^{1,3}$, we can merge a pair of Weyl nodes to realize the 1st- or 2nd-order WSMs. The plus and minus signs denote the monopole charges, and the green arrowed lines and cyan dotted lines denote the surface arcs and hinge arcs, respectively.

Heuristically, Eq. (1) can be viewed as a family of 2D QIs having intra-cell coupling amplitudes parameterized by k_z: $\gamma(k_z) = \gamma + \frac{1}{2}\cos(k_z)$ [1]. The phase diagram of the QI is shown in the upper panel of Fig. 1(b), where we see that when $\gamma = -1$ then $-1.5 < \gamma(k_z) < -0.5$, and the 2D QI transits between the trivial phase and the topological phase having a quantized quadrupole moment $Q_{xy} = \frac{1}{2}$ as k_z traverses through the Brillouin zone (BZ). This family of 2D QIs represents a 3D HODSM which hosts two 3D Dirac nodes, one each at $k_z = \pm\arccos[-2(1+\gamma)]$, corresponding to the phase transition points [where $\gamma(k_z) = -1$] between a 2D trivial and a 2D quadrupolar phase protected by C_4^z.

Interestingly, by breaking certain symmetries, we can split these Dirac nodes and realize various HOWSMs as shown in Figs. 1(c)–1(e). We first consider $H^1 = H_{\mathrm{HODSM}} + m_1 i\Gamma_1\Gamma_3$, which breaks time-reversal symmetry $\mathcal{T}$, $\mathcal{M}_x$, and $\mathcal{M}_y$, but preserves C_4^z, $\mathcal{M}_x\mathcal{T}$, $\mathcal{M}_y\mathcal{T}$, and $\mathcal{I}$. The perturbation $i\Gamma_1\Gamma_3$ gaps out or splits the original phase transition point at $\gamma(k_z) = -1$ into two transitions, and generates a new Chern insulator phase ($C = 1$) bounded by the new critical points at $\gamma(k_z) = -1 \pm [(|m_1|)/(\sqrt{2})]$ [see the lower panel of Fig. 1(b)]. Thus, in the 3D system the bulk Dirac nodes are split into two Weyl nodes.

For this perturbation, there exist four Weyl nodes, Fig. 2(a), at $k_z = \pm\arccos[-2 \pm \sqrt{2}m_1 - 2\gamma]$ which are connected through surface Fermi arcs as shown in Fig. 2(b). Remarkably, when cutting the surface again to form hinges, the two Weyl nodes closest to $k_z = 0$ are connected by additional hinge arcs, as depicted in Fig. 2(c), indicating that they are 2nd-order Weyl nodes that act as the critical point (as a function of k_z) between a Chern insulator, and a QI having vanishing Chern number. Since this HOWSM consists of both 1st- and 2nd-order Weyl nodes [as of Figs. 2(a)–2(d)], we can call it a hybrid-order Weyl semimetal.

To characterize the higher-order topology we can calculate the bulk quadrupole moment $q_{xy}(k_z)$ for each k_z slice [49]. Figure 2(d) shows that $q_{xy}(k_z)$ is quantized to a nontrivial value of $-\frac{1}{2}$ for the k_z range where the hinge arcs exist. Therefore, the hinge states of H^1 can be captured by a second-order topological invariant. We can merge the 1st-order (2nd-order) Weyl nodes independently in H^1 by increasing (decreasing) γ to transition the system to a 2nd-order WSM (1st-order WSM) [see Figs. 2(e)–2(h)]. The merging of Weyl nodes can be understood using the phase diagram shown in the lower panel of Fig. 1(b). By tuning γ, the trajectory of $\gamma(k_z)$ shifts horizontally; when the trajectory crosses only critical points separating a trivial phase and a $C = 1$ phase, the corresponding 3D WSM hosts 1st-order Weyl nodes, while for critical points separating a $C = 1$ and the QI phase, the 3D WSM hosts 2nd-order Weyl nodes.

Unlike the 1st-order Weyl nodes, which separate two phases having different Chern numbers, the 2nd-order Weyl node requires one of the two separated phases to have a

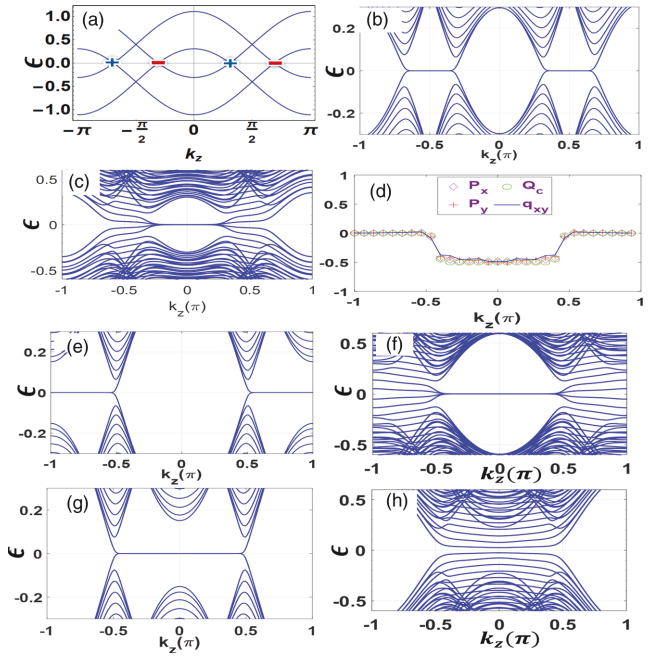

FIG. 2. (a) Bulk band structure of H^1_{HOWSM} along k_z for $k_x = k_y = 0$. (b) Surface Fermi arcs connecting bulk nodes. (c) Hinge Fermi arcs connecting the two middle nodes (higher-order nodes) (d) The combined plot of $P_x(k_z)$, $P_y(k_z)$, $Q_c(k_z)$, and $q_{xy}(k_z)$ showing the nonzero quantized quadrupole moment corresponding to the region having hinge arcs [$\gamma = -1$, $m_1 = 0.4$, used in (a)–(d)]. (e) Surface and (f) hinge spectrum for a 2nd-order WSM ($\gamma = -0.7$, $m_1 = (0.6/\sqrt{2})$, Weyl nodes at $k_z = \pm(\pi/2)$). (g) Surface and (h) hinge spectrum for a 1st-order WSM ($\gamma = -1.3$, $m_1 = (0.6/\sqrt{2})$, Weyl nodes at $k_z = \pm(\pi/2)$).

nonzero quantized higher-order invariant, which usually necessitates the Chern number to vanish in that phase. In C_4 symmetric systems, both the Chern number (modulo 4) and the quadrupole moment can be determined by the symmetry representations of the C_4^z operator formed by occupied bands at the high symmetry points in the BZ [2,50,51]. These symmetry indicators can therefore be used as a bulk diagnosis for 2nd-order Weyl nodes (see Supplemental Material [52]). However, it is important to note that in order to characterize the 2nd-order nodes, the symmetry indicators of just the two crossing bands are not sufficient [53], therefore the other occupied bands need to be considered to determine the order of the node.

From Fig. 2(c), we see that hinge arcs in the HOWSM emanate from the projections of the bulk nodes on the hinges. However, unlike the surface arcs, the hinge arcs are protected by C_4^z symmetry and, while their degeneracy is protected, their energies can be pushed outside of the midgap region. It may be difficult to precisely control the energies of the hinge modes in electronic materials. However, it is typically straightforward to manipulate the energies of boundary modes in metamaterial contexts by modifying the effective boundary conditions. Finally, even if the hinge modes are completely removed one can still generically use fractional charge density on the hinges as a measure of the higher order topology [6,54,55].

As a second example of a HOWSM we can consider a model in which we add the same perturbation in H^1, but with an explicit momentum dependence: $H^2(\mathbf{k}) = H_{\mathrm{HODSM}}(\mathbf{k}) + m_2 \sin(k_z) i\Gamma_1\Gamma_3$. This has the effect of restoring $\mathcal{T}$ while maintaining C_4^z. In contrast to $\mathcal{T}$-broken WSMs, in the presence of $\mathcal{T}$ due to the requirement of the minimum number of four nodes, interestingly, the 1st- or 2nd-order pairs cannot be merged separately and forced to coexist. Instead, by tuning γ, all of the nodes merge to gap out, as illustrated in Fig. 1(d) [56].

So far, we have realized two HOWSMs with C_4^z symmetry where all Weyl nodes are aligned along the high symmetry line $(k_x, k_y) = (0, 0)$. We now show that one can realize HOWSMs where nodes are split in other planes by applying a different perturbation to Eq. (1). Consider $H^3(\mathbf{k}) = H_{\mathrm{HODSM}}(\mathbf{k}) + m_3 \sin(k_z) i\Gamma_2\Gamma_3$, which explicitly breaks $\mathcal{M}_z$ and $\mathcal{T}$, but preserves $\mathcal{I}$. Since $\mathcal{M}_x$ is also broken, but $\mathcal{M}_y$ is preserved, the Dirac nodes split in only the $k_y - k_z$ plane. As a result, there are now surface Fermi arcs connecting nodes split in the k_y direction. Since we have $\mathcal{I}$ symmetry the four nodes form two parallel dipoles of monopole charges [see Fig. 1(e)]. Unlike $H^{1,2}$, the surface and hinge arcs of H^3 are perpendicular to each other [see Figs. 1(d), 1(e) for a schematic illustration and Ref. [52] for a plot of the spectrum]. We find that the higher-order topology can still be characterized using the quadrupole moment [57]. Finally, in addition to these three examples, we note that we considered models of HOWSMs having various arrangements of Weyl nodes possessing hinge states which belong to the category of "extrinsic HOWSMs" [58] (see Supplemental Material [52] for details and Ref. [21] for an example of higher-order Weyl superconductor).

Hybridizing 1st- and 2nd-order WSMs.—What are the physical consequences of 2nd-order nodes and how they interplay with the 1st-order nodes? Since the 2nd-order nodes can manifest boundary features beyond surface arcs, it is natural to ask what will happen when we couple Weyl nodes of different orders. As a proof of concept, let us consider coupling the 2nd-order WSM in Figs. 2(e), 2(f) with the 1st-order WSM in Figs. 2(g), 2(h). Both phases are generated from the same model, but have different values of γ. In order to gap out the bulk nodes, we change $\gamma(k_z)$ in Eq. (1) to $\gamma(k_z + \pi)$ for the 1st-order WSM, and reverse the sign of the perturbation m_1 such that its surface Fermi arcs overlap with the surface arcs in the 2nd-order WSM in Fig. 2(e). Then, the Hamiltonian of the hybridized system is

$$h_{1\&2} = \begin{bmatrix} H_{\mathrm{WSM}}(-m_1, k_z + \pi) & t\hat{T} \\ t^*\hat{T}^\dagger & H^1_{\mathrm{HOWSM}}(m_1, k_z) \end{bmatrix}, \quad (2)$$

where $\hat{T}$ is the hybridization matrix which couples the two Weyl phases, and t is the coupling strength.

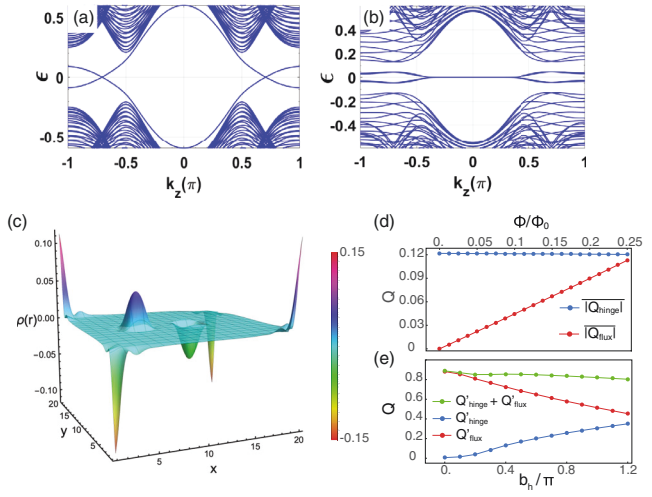

FIG. 3. (a) The surface and (b) hinge spectrum of the hybrid topological insulator $h_{1\&2}$. Electromagnetic response of HOWSMs: (c) Charge density at half-filling for H^1_{HOWSM} having localized magnetic flux along z and open boundary condition along x and y. (d),(e) Change in hinge charge and flux charge by (d) tuning magnetic field and (e) the length of the hinge arc. $Q'_{\mathrm{hinge}} = (2Q_{\mathrm{hinge}}/e)$, $Q'_{\mathrm{flux}} = Q_{\mathrm{flux}}(\Phi_0/e\Phi_z)$.

To form an insulating phase we need to choose $\hat{T}$ such that the bulk nodes are hybridized and gapped. We find that the only $\hat{T}$ that can fully gap out the bulk nodes is $\hat{T} = \sigma^0\kappa^2 = i\Gamma_1\Gamma_3$. As shown in Figs. 3(a), 3(b), this insulating phase of $h_{1\&2}$ is a hybrid-order topological insulator with coexisting surface Dirac cone pairs and flatband hinge states where the former are protected by the combination of $\mathcal{M}_x\mathcal{T}$ and $\mathcal{M}_y\mathcal{T}$ symmetries, and the latter protected by C_4^z as before. Remarkably, the hinge states do not originate from the surface cones as occurs in graphene, for example, or in the quadrupolar surface semimetals shown in Ref. [39]. Instead, they are protected by independent symmetries and can be gapped out independently. For example, one can break C_4^z while preserving $\mathcal{M}_x\mathcal{T}, \mathcal{M}_y\mathcal{T}$ to remove the hinge states (see Ref. [52]). This leads to a type of hybrid-order topology which to our knowledge has not been reported elsewhere. The unusual hybrid-order TI arising form the combination of 1st-order and 2nd-order WSMs allows us to use the coupling to conventional WSMs as a means to detect the higher-order topology of a 2nd-order WSM.

The 1st- and 2nd-order Weyl-CDW.—It is known [59–64] that a charge-density wave order can gap out the Weyl nodes and induce an insulating phase with an axionic field. Here, we study the nesting of both $\mathcal{I}$- and $\mathcal{T}$-symmetric Weyl-CDW ($\mathcal{I}$- and $\mathcal{T}$-Weyl CDW) in the lattice models of the 1st-order and 2nd-order WSMs, separately. For the 1st-order $\mathcal{I}$-Weyl-CDW we find that the resulting gapped phase has nonvanishing Chern number for all k_z slices leading to gapless surface states across the whole BZ. Therefore, different from the prediction of the low-energy field theory, the lattice model of a nested Weyl-CDW results in a stacked Chern insulator [65]. However, for the case of 2nd-order $\mathcal{I}$-Weyl CDW, remarkably, we find an insulating phase with a coexistence of the surface and flatband hinge states throughout the BZ (see Supplemental Material [52] for details). In another words, a 2nd-order $\mathcal{I}$-Weyl CDW can be thought as a stack of hybrid-topology TIs. Next, we turn to $\mathcal{T}$-Weyl-CDW, where as mentioned before the 1st- and 2nd-order nodes are forced to coexist. As a result, interestingly, inducing a CDW order, unlike the $\mathcal{I}$-Weyl CDW, gaps out a 2nd-order node by a 1st-order node. A phenomena which uniquely distinguishes the $\mathcal{T}$-HOWSMs from their conventional counterpart and make them a natural platform for the investigation of interplay of 1st- and 2nd-order Weyl nodes in equal footing. We find that the resulting gapped $\mathcal{T}$-Weyl CDW is a 3D hybrid TI with coexisting surface Dirac cone and hinge arcs [52]. Therefore, we demonstrated that 2nd-order nodes behave very distinctively when they are gapped out either through the coupling to a conventional (1st-order) WSM or via nesting to another 1st- or 2nd-order node by a CDW order, which could be of great help for the future experimental investigation of these new classes of materials.

Electromagnetic response of 2nd-order Weyl nodes.—We will now show that 2nd-order WSMs can show an interesting electromagnetic response as a result of the coexistence of surface and hinge Fermi arcs. Let us consider the case of H^1 in a regime where we have two 2nd-order Weyl nodes located on the k_z axis. It is known that the charge response in conventional WSMs manifests as $\rho = (e^2\mathbf{b}_s \cdot \mathbf{B}/4\pi^2)$ [66–68], where $\mathbf{b}_s$ is the vector connecting the two Weyl nodes.

Hence, the charge per layer along $\hat{z}$ in the presence of a magnetic flux is $|Q_f| = |(b_s/2\pi)(e\Phi_z/\Phi_0)|$ which is proportional to the flux strength ($\Phi_z/\Phi_0 = e\Phi_z/h$) for the applied magnetic field in the z direction, and the nodal separation along k_z [66]. Simultaneously, for a system with open boundary conditions in the x and y directions we also expect localized fractional charge at the hinges parallel to $\hat{z}$, whose value is proportional to the (momentum-space) length of the hinge arcs, b_h: $|Q_h| = |(b_h/2\pi)(e/2)|$. In the case of minimal models having only two (2nd-order) Weyl nodes separated along the k_z axis, the length of hinge, and the surface arcs together must span the whole BZ, i.e., $b_s + b_h = 2\pi$ or, equivalently, $|Q_f|(\Phi_0/e\Phi_z) + |Q_h|(2/e) = 1$. For example, if we insert one flux quantum this yields the remarkable result $|Q_f| + 2|Q_h| = e$ independent of the other details of the system.

To confirm these charge distributions numerically let us take the model of H^1 in Figs. 2(e), 2(f) and insert two oppositely oriented flux lines localized in the xy plane. The charge density at half filling in Fig. 3(c) shows the charge accumulation at both the fluxes and the hinges. While the charge bound to the flux is proportional to the external flux, the hinge charge is insensitive to it, as shown in Fig. 3(d). However, due to the constraint on b_s and b_h for this two-node WSM there is a competition between the hinge and

flux charges as shown in Fig. 3(e). Namely, for a fixed amount of flux, increasing the length of the hinge arcs in H^1, increases Q_h but decreases Q_f; while the weighted sum of Q_h and Q_f remains constant during this process. Thanks to the recent developments in charge measurement analogs in metamaterials [54] we expect this property can serve as an experimental indicator for the HOWSM phase in those contexts, and possibly in electronic materials.

Type-II and hybrid higher-order Weyl semimetals.—We can extend the models introduced here (we only show this for the model H^1) to introduce higher-order type-II [47,69] and hybrid-tilt Weyl phases [48,70]. This can be done by including a term proportional to the identity matrix: $\alpha \sin(k_z - \theta)\mathbb{I}_4$. For $\theta = \pi/2$, and for a sufficiently strong α, the Weyl nodes undergo a transition to type-II nodes (see Supplemental Material [52]). Furthermore, by tuning θ to a small value, the nodal tilt can be tuned to form a hybrid-tilt Weyl phase. Therefore, this model can realize a complete set of type-I, type-II, and hybrid-tilt phases having 1st-, 2nd-, and hybrid-order topology.

Possible experimental realization.—The 2D QI model proposed in Ref. [1] is already experimentally realized in multiple metamaterial contexts [9–11,13]. In light of these developments, building a metamaterial HODSM as in Eq. (1) constructed from a stack of 2D QI layers is feasible. Moreover, solid-state candidates were recently proposed to be HODSMs, e.g., the room- (α) and intermediate-temperature (α") phases of Cd_3As_2, KMgBi, and rutile structure (β'-) PtO_2 [42,46]. Moreover, periodic driving has already proven useful in inducing Weyl phases in conventional topological semimetals [70–73]. Here we obtain a time-independent Hamiltonian for a circularly polarized light in the high-frequency limit [74] which can split the two Dirac nodes into four Weyl nodes on the k_z axis (see Ref. [52]). Therefore, we expect that driving the HODSM in Eq. (1) using circular polarized light can produce the same physics as H^1. Soon after our paper appeared on arXiv, two other articles [75,76] related to higher-order Weyl semimetals appeared on arXiv.

S. A. A. G. thanks ARO (Grant No. W911NF-18-1-0290) and NSF (Grant No. DMR1455233) for support. T. L. thanks the U.S. National Science Foundation (NSF) MRSEC program under NSF Grant No. DMR-1720633 (SuperSEED) for support. T. L. H. thanks the U.S. Office of Naval Research (ONR) Multidisciplinary University Research Initiative (MURI) Grant No. N00014-20-1-2325 on Robust Photonic Materials with High-Order Topological Protection.

*sghorashi@wm.edu

[1] W. A. Benalcazar, B. A. Bernevig, and T. L. Hughes, Quantized electric multipole insulators, Science **357**, 61 (2017).

[2] W. A. Benalcazar, B. A. Bernevig, and T. L. Hughes, Selected for a viewpoint in physics electric multipole moments, topological multipole moment pumping, and chiral hinge states in crystalline insulators, Phys. Rev. B **96**, 245115 (2017).

[3] Z. Song, Z. Fang, and C. Fang, $(d-2)$-Dimensional Edge States of Rotation Symmetry Protected Topological States, Phys. Rev. Lett. **119**, 246402 (2017).

[4] F. Schindler, A. M. Cook, M. G. Vergniory, Z. Wang, S. S. P. Parkin, B. A. Bernevig, and T. Neupert, Higher-order topological insulators, Sci. Adv. **4**, eaat0346 (2018).

[5] J. Langbehn, Y. Peng, L. Trifunovic, F. von Oppen, and P. W. Brouwer, Reflection-Symmetric Second-Order Topological Insulators and Superconductors, Phys. Rev. Lett. **119**, 246401 (2017).

[6] W. A. Benalcazar, T. Li, and T. L. Hughes, Quantization of fractional corner charge in C_n-symmetric higher-order topological crystalline insulators, Phys. Rev. B **99**, 245151 (2019).

[7] S. A. A. Ghorashi, T. L. Hughes, and E. Rossi, Vortex and Surface Phase Transitions in Superconducting Higher-Order Topological Insulators, Phys. Rev. Lett. **125**, 037001 (2020).

[8] T. Li, P. Zhu, W. A. Benalcazar, and T. L. Hughes, Fractional disclination charge in two-dimensional C_n-symmetric topological crystalline insulators, Phys. Rev. B **101**, 115115 (2020).

[9] M. Serra-Garcia, V. Peri, R. Süsstrunk, O. R. Bilal, T. Larsen, L. G. Villanueva, and S. D. Huber, Observation of a phononic quadrupole topological insulator, Nature (London) **555**, 342 (2018).

[10] C. W. Peterson, W. A. Benalcazar, T. L. Hughes, and G. Bahl, A quantized microwave quadrupole insulator with topologically protected corner states, Nature (London) **555**, 346 (2018).

[11] J. Noh, W. A. Benalcazar, S. Huang, M. J. Collins, K. P. Chen, T. L. Hughes, and M. C. Rechtsman, Topological protection of photonic mid-gap defect modes, Nat. Photonics **12**, 408 (2018).

[12] F. Schindler, Z. Wang, M. G. Vergniory, A. M. Cook, A. Murani, S. Sengupta, A. Yu. Kasumov, R. Deblock, S. Jeon, I. Drozdov, H. Bouchiat, S. Guéron, A. Yazdani, B. A. Bernevig, and T. Neupert, Higher-order topology in bismuth, Nat. Phys. **14**, 918 (2018).

[13] S. Imhof, C. Berger, F. Bayer, J. Brehm, L. W. Molenkamp, T. Kiessling, F. Schindler, C. H. Lee, M. Greiter, T. Neupert, and R. Thomale, Topolectrical-circuit realization of topological corner modes, Nat. Phys. **14**, 925 (2018).

[14] H. Xue, Y. Yang, F. Gao, Y. Chong, and B. Zhang, Acoustic higher-order topological insulator on a Kagome lattice, Nat. Mater. **18**, 108 (2019).

[15] X. Ni, M. Weiner, A. Alù, and A. B Khanikaev, Observation of higher-order topological acoustic states protected by generalized chiral symmetry, Nat. Mater. **18**, 113 (2019).

[16] H. Li and K. Sun, Pfaffian Formalism for Higher-Order Topological Insulators, Phys. Rev. Lett. **124**, 036401 (2020).

[17] K. Kudo, T. Yoshida, and Y. Hatsugai, Higher-Order Topological Mott Insulators, Phys. Rev. Lett. **123**, 196402 (2019).

[18] R.-X. Zhang, W. S. Cole, X. Wu, and S. D. Sarma, Higher-Order Topology and Nodal Topological Superconductivity in Fe(Se,Te) Heterostructures, Phys. Rev. Lett. **123**, 167001 (2019).

[19] Z. Yan, Higher-Order Topological Odd-Parity Superconductors, Phys. Rev. Lett. **123**, 177001 (2019).

[20] A. Tiwari, M.-H. Li, B. A. Bernevig, T. Neupert, and S. A. Parameswaran, Unhinging the Surfaces of Higher-Order Topological Insulators and Superconductors, Phys. Rev. Lett. **124**, 046801 (2020).

[21] R.-X. Zhang, Y.-T. Hsu, and S. D. Sarma, Higher-order topological dirac superconductors, Phys. Rev. B **102**, 094503 (2020).

[22] S.-B. Zhang and B. Trauzettel, Detection of second-order topological superconductors by Josephson junctions, Phys. Rev. Research **2**, 012018 (2020).

[23] O. Dubinkin, J. May-Mann, and T. L. Hughes, Lieb Schultz Mattis-type theorems and other non-perturbative results for strongly correlated systems with conserved dipole moments, arXiv:2001.04477.

[24] Y. You, T. Devakul, F. J. Burnell, and T. Neupert, Higher-order symmetry-protected topological states for interacting bosons and fermions, Phys. Rev. B **98**, 235102 (2018).

[25] O. Dubinkin and T. L. Hughes, Higher-order bosonic topological phases in spin models, Phys. Rev. B **99**, 235132 (2019).

[26] M. J. Park, Y. Kim, G. Y. Cho, and S. B. Lee, Higher-Order Topological Insulator in Twisted Bilayer Graphene, Phys. Rev. Lett. **123**, 216803 (2019).

[27] R. Queiroz, I. C. Fulga, N. Avraham, H. Beidenkopf, and J. Cano, Partial Lattice Defects in Higher-Order Topological Insulators, Phys. Rev. Lett. **123**, 266802 (2019).

[28] Q.-B. Zeng, Y.-B. Yang, and Y. Xu, Higher-order topological insulators and semimetals in generalized Aubry-André-harper models, Phys. Rev. B **101**, 241104(R) (2020).

[29] M. Kheirkhah, Y. Nagai, C. Chen, and F. Marsiglio, Majorana corner flat bands in two-dimensional second-order topological superconductors, Phys. Rev. B **101**, 104502 (2020).

[30] C.-H. Hsu, P. Stano, J. Klinovaja, and D. Loss, Majorana Kramers Pairs in Higher-Order Topological Insulators, Phys. Rev. Lett. **121**, 196801 (2018).

[31] M. Kheirkhah, Z. Yan, Y. Nagai, and F. Marsiglio, First- and Second-Order Topological Superconductivity and Temperature-Driven Topological Phase Transitions in the Extended Hubbard Model with Spin-Orbit Coupling, Phys. Rev. Lett. **125**, 017001 (2020).

[32] Z. Yan, F. Song, and Z. Wang, Majorana Corner Modes in a High-Temperature Platform, Phys. Rev. Lett. **121**, 096803 (2018).

[33] Q. Wang, C.-C. Liu, Y.-M. Lu, and F. Zhang, High-Temperature Majorana Corner States, Phys. Rev. Lett. **121**, 186801 (2018).

[34] Z. Yan, Higher-Order Topological Odd-Parity Superconductors, Phys. Rev. Lett. **123**, 177001 (2019).

[35] B. Roy, Antiunitary symmetry protected higher-order topological phases, Phys. Rev. Research **1**, 032048 (2019).

[36] N. Bultinck, B. A. Bernevig, and M. P. Zaletel, Three-dimensional superconductors with hybrid higher-order topology, Phys. Rev. B **99**, 125149 (2019).

[37] S. H. Kooi, G. van Miert, and C. Ortix, The hybrid-order topology of weak topological insulators, Phys. Rev. B **102**, 041122 (2020).

[38] S. A. A. Ghorashi, X. Hu, T. L. Hughes, and E. Rossi, Second-order dirac superconductors and magnetic field induced Majorana hinge modes, Phys. Rev. B **100**, 020509(R) (2019).

[39] M. Lin and T. L. Hughes, Topological quadrupolar semimetals, Phys. Rev. B **98**, 241103(R) (2018).

[40] D. Călugăru, V. Juričić, and B. Roy, Higher-order topological phases: A general principle of construction, Phys. Rev. B **99**, 041301(R) (2019).

[41] M. Ezawa, Higher-Order Topological Insulators and Semimetals on the Breathing Kagome and Pyrochlore Lattices, Phys. Rev. Lett. **120**, 026801 (2018).

[42] B. J. Wieder, Z. Wang, J. Cano, X. Dai, L. M. Schoop, B. Bradlyn, and B. A. Bernevig, Strong and fragile topological Dirac semimetals with higher-order Fermi arcs, Nat. Commun. **11** (2020), 627.

[43] M. Ezawa, Second-order topological insulators and loop-nodal semimetals in transition metal dichalcogenides $x\mathrm{te}_2$ ($x = \mathrm{Mo}, \mathrm{W}$), Sci Rep. **9**, 1 (2019).

[44] A. Szabo and B. Roy, Dirty higher-order dirac semimetal: Quantum criticality and bulk-boundary correspondence, Phys. Rev. Research **2**, 043197 (2020).

[45] Z. Wang, B. J. Wieder, J. Li, B. Yan, and B. A. Bernevig, Higher-Order Topology, Monopole Nodal Lines, and the Origin of Large Fermi Arcs in Transition Metal Dichalcogenides $x\mathrm{te}_2$ ($x = \mathrm{Mo}, \mathrm{W}$), Phys. Rev. Lett. **123**, 186401 (2019).

[46] C.-Z. Li, A.-Q. Wang, C. Li, W.-Z. Zheng, A. Brinkman, D.-P. Yu, and Z.-M. Liao, Reducing Electronic Transport Dimension to Topological Hinge States by Increasing Geometry Size of Dirac Semimetal Josephson Junctions, Phys. Rev. Lett. **124**, 156601 (2020).

[47] N. P. Armitage, E. J. Mele, and A. Vishwanath, Weyl and Dirac semimetals in three-dimensional solids, Rev. Mod. Phys. **90**, 015001 (2018).

[48] F.-Y. Li, X. Luo, X. Dai, Y. Yu, F. n Zhang, and G. Chen, Hybrid Weyl semimetal, Phys. Rev. B **94**, 121105(R) (2016).

[49] Using $q_{xy}(k_z) \equiv [P_x(k_z) + P_y(k_z) - Q_c(k_z)]\mathrm{mod}1$ [1,2,39], where $P_x(k_z)[P_y(k_z)]$ is the $x(y)$ component of the polarization localized at the $y(x)$ surface, and $Q_c(k_z)$ is the corner charge.

[50] C. Fang, M. J. Gilbert, and B. A. Bernevig, Bulk topological invariants in noninteracting point group symmetric insulators, Phys. Rev. B **86**, 115112 (2012).

[51] W. A. Benalcazar, J. C. Y. Teo, and T. L. Hughes, Classification of two-dimensional topological crystalline superconductors and Majorana bound states at disclinations, Phys. Rev. B **89**, 224503 (2014).

[52] See Supplemental Material at http://link.aps.org/supplemental/10.1103/PhysRevLett.125.266804 for details on (i) C_4^z-symmetry indicators of 2nd-order Weyl nodes, (ii) effective surface Hamiltonian, (iii) surface and hinge spectrum of $H^{2,3}$, (iv) some models of extrinsic HOWSMs, (v) hybridization of 1st- and 2nd-order nodes, (vi) nesting of 1st- and 2nd-order nodes by CDW, (vii) Floquet HOWSMs, (ix) experimental considerations, (x) HOWSMs from spinful HODSMs.

[53] Another way to understand this is to notice that the low-energy descriptions (e.g., $k \cdot P$) of 1st- and 2nd-order nodes are identical.
[54] C. W. Peterson, T. Li, W. A. Benalcazar, T. L. Hughes, and G. Bahl, A fractional corner anomaly reveals higher-order topology, Science **368**, 1114 (2020).
[55] C. W. Peterson, T. Li, W. Jiang, T. L. Hughes, and G. Bahl, Observation of trapped fractional charge and topological states at disclination defects in higher-order topological insulators, arXiv:2004.11390.
[56] This has particularly interesting implications for experimental investigation of $\mathcal{T}$-symmetric HOWSM. Moreover, note that unlike the surface arcs of the conventional WSMs, the hinge arcs of HOWSM can connect two nodes with the same monopole charges [Fig. 1(d)] as they are perfect flatbands and do not carry any chirality.
[57] This is well defined since M_y quantizes the quadrupole moment, while the polarization is quantized by $\mathcal{I}$, and vanishes for this parameter regime.
[58] M. Geier, L. Trifunovic, M. Hoskam, and P. W. Brouwer, Second-order topological insulators and superconductors with an order-two crystalline symmetry, Phys. Rev. B **97**, 205135 (2018).
[59] K.-Y. Yang, Y.-M. Lu, and Y. Ran, Quantum Hall effects in a Weyl semimetal: Possible application in pyrochlore iridates, Phys. Rev. B **84**, 075129 (2011).
[60] Z. Wang and S.-C. Zhang, Chiral anomaly, charge density waves, and axion strings from Weyl semimetals, Phys. Rev. B **87**, 161107(R) (2013).
[61] Y. You, G. Y. Cho, and T. L. Hughes, Response properties of axion insulators and Weyl semimetals driven by screw dislocations and dynamical axion strings, Phys. Rev. B **94**, 085102 (2016).
[62] J. Gooth, B. Bradlyn, S. Honnali, C. Schindler, N. Kumar, J. Noky, Y. Qi, C. Shekhar, Y. Sun, Z. Wang *et al.*, Axionic charge-density wave in the Weyl semimetal (TASe 4) 2 i, Nature (London) **575**, 315 (2019).
[63] H. Wei, S.-P. Chao, and V. Aji, Excitonic Phases from Weyl Semimetals, Phys. Rev. Lett. **109**, 196403 (2012).
[64] B. J. Wieder, K.-S. Lin, and B. Bradlyn, Is the dynamical axion Weyl-charge-density wave an axionic band insulator?, Phys. Rev. Research **2**, 042010 (2020).
[65] See Ref. [52] for the details. Also during the preparation of this work, we became aware of Ref. [64] on the conventional (1st-order) Weyl-CDW which they also found a stack of Chern insulators.
[66] M. M. Vazifeh and M. Franz, Electromagnetic Response of Weyl Semimetals, Phys. Rev. Lett. **111**, 027201 (2013).
[67] A. A. Burkov and L. Balents, Weyl Semimetal in a Topological Insulator Multilayer, Phys. Rev. Lett. **107**, 127205 (2011).
[68] X. Wan, A. M. Turner, A. Vishwanath, and S. Y. Savrasov, Topological semimetal and fermi-arc surface states in the electronic structure of pyrochlore iridates, Phys. Rev. B **83**, 205101 (2011).
[69] A. A. Soluyanov, D. Gresch, Z. Wang, Q. S. Wu, M. Troyer, X. Dai, and B. A. Bernevig, Type-ii Weyl semimetals, Nature (London) **527**, 495 (2015).
[70] S. A. A. Ghorashi, Hybrid dispersion Dirac semimetal and hybrid Weyl phases in Luttinger semimetals: A dynamical approach, Ann. Phys. (Amsterdam) **532**, 1900336 (2020).
[71] H. Hubener, M. A. Sentef, U. De Giovannini, A. F. Kemper, and A. Rubio, Creating stable Floquet–Weyl semimetals by laser-driving of 3d Dirac materials, Nat. Commun. **8**, 13940 (2017).
[72] S. A. A. Ghorashi, P. Hosur, and C.-S. Ting, Irradiated three-dimensional luttinger semimetal: A factory for engineering Weyl semimetals, Phys. Rev. B **97**, 205402 (2018).
[73] T. Oka and S. Kitamura, Floquet engineering of quantum materials, Annu. Rev. Condens. Matter Phys. **10**, 387 (2019).
[74] $h_{\mathrm{eff}}^{W1}(\boldsymbol{k}) = H_{\mathrm{HODSM}}(\boldsymbol{k}) + (iA_0^2\eta/2\omega)\{\sin(k_x)\sin(ky)[\Gamma_2,\Gamma_4] - [\Gamma_1,\Gamma_4]\sin(k_x) - [\Gamma_2,\Gamma_3]\sin(k_y) + [\Gamma_1,\Gamma_3]\}$, where $A_0 \propto E/\omega$, E is the electric field, and $\eta = \pm 1$ is the chirality of the light. At $k_x = k_y = 0$, the effect of light is $\propto i\Gamma_1\Gamma_3$.
[75] H-X. Wang, Z-K. Lin, B. Jiang, G.-Y. Guo, and J.-H. Jiang, Higher-Order Weyl Semimetals, Phys. Rev. Lett. **125**, 146401 (2020).
[76] Q. Wei, X. Zhang, W. Deng, J. Lu, X. Huang, M. Yan, G. Chen, Z. Liu, and S. Jia, Higher-order topological semimetal in phononic crystals, arXiv:2007.03935.